Joule

CellPress

Article

Efficient Perovskite Solar Modules with Minimized Nonradiative Recombination and Local Carrier Transport Losses

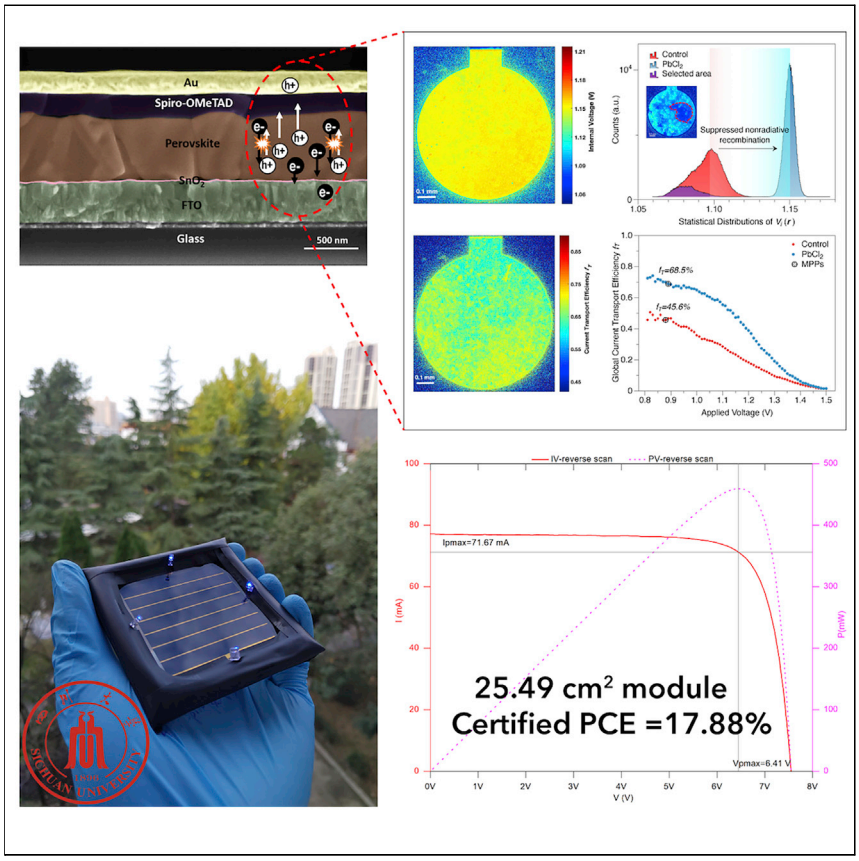

We have developed quantitative and spatially resolved imaging techniques to identify the origin of nonradiative-radiative recombination and carrier transport losses in perovskite solar cells, offering potential for future real-time tracking of the lab-scaled devices and fast assessment of screening the large-area modules. By dual-chloride passivation strategy, the resulting 25.49 cm^2 perovskite solar module achieves a certified power conversion efficiency of 17.88%.

Aobo Ren, Huagui Lai, Xia Hao, ..., Masakazu Sugiyama, Jiang Wu, Dewei Zhao

hao.xia0808@scu.edu.cn (X.H.)
dewei.zhao@scu.edu.cn (D.Z.)

HIGHLIGHTS

A strategy to identify the nonradiative recombination and carrier transport losses

Significant reduction in nonradiative voltage loss from 0.165 to 0.116 V

25.49 cm^2 perovskite solar module with a 17.88%-certified PCE and a record FF over 78%

Ren et al., Joule 4, 1263–1277
June 17, 2020
https://doi.org/10.1016/j.joule.2020.04.013

Joule

CellPress

Article

Efficient Perovskite Solar Modules with Minimized Nonradiative Recombination and Local Carrier Transport Losses

Aobo Ren,[1,2,5] Huagui Lai,[1,5] Xia Hao,[1,*] Zeguo Tang,[3] Hao Xu,[4] Bernice Mae F. Yu Jeco,[4] Kentaroh Watanabe,[4] Lili Wu,[1] Jingquan Zhang,[1] Masakazu Sugiyama,[4] Jiang Wu,[2] and Dewei Zhao[1,6,*]

SUMMARY

Perovskite solar cells (PSCs) have seen rapid advance in power conversion efficiencies (PCEs). However, the state-of-the-art PSCs still suffer from inhomogeneously distributed nonradiative recombination and carrier transport losses. Here, we report a promising evaluation strategy of combining the generalized optoelectronic reciprocity theorems and camera-based luminescence imaging techniques for PSCs. Excess lead chloride compositional engineering increases homogeneity and suppresses nonradiative recombination, leading to an external luminescence efficiency of 1.14% of devices (corresponding to a nonradiative voltage loss of 0.116 V). A favorable local and global carrier extraction property at maximum power point is also observed under moderate illumination level. As a result, we achieve a 25.49 cm^2 perovskite solar module with a 17.88%-certified efficiency and a record fill factor over 78%. This quantitative and spatially resolved characterization is applicable at specific operating points, offering enormous potential for future real-time tracking of the lab-scaled devices and fast assessment of screening the large-area modules.

INTRODUCTION

Perovskite solar cells (PSCs) have recently attracted great attention due to their power conversion efficiency (PCE) rapidly exceeding 25%,[1] in which the perovskite absorber has a typical ABX_3 structure, where A (methylammonium [MA] = $CH_3NH_3^+$ and formamidinium [FA] = $CH_3(NH_2)_2^+$), B (Pb^{2+}, Sn^{2+}, and Ge^{2+}), and X (I^-, Br^-, and Cl^-) are organic cations, divalent metals, and anions, respectively.[2–9] Most of high-performance PSCs adopt a mixture of triple cations including FA, MA, and cesium (Cs).[10] Although triple-cation Cs/FA/MA has been proved to promote uniform perovskite films with better thermal stability and less phase impurities, the device performance is still far from the expected.

Generally, Shockley-Queisser (SQ) limit predicts the highest theoretical efficiency for single-junction solar cells, on the assumption that the recombination of electron-hole pairs is only radiative.[11] In a real solar cell, losses take place due to the nonradiative recombination and ineffective carrier transport.[12] The former reduces the non-equilibrium carrier concentrations in both energy bands, leading to reduction in the quasi-Fermi levels splitting and the maximum open-circuit voltage (V_{OC}).[13,14] The latter denotes the losses during the aggregation of junction carriers into the terminals. Specifically, the V_{OC} of triple-cation PSCs is generally limited to

Context & Scale

Power conversion efficiencies of perovskite solar cells (PSCs) have been rapidly boosted in the past decade. However, the state-of-the-art PSCs are still suffering from inhomogeneously distributed nonradiative recombination and carrier transport losses. Eliminating nonradiative recombination and carrier transport losses plays significant roles in achieving high-performance devices. Previous studies evaluating the passivation effect and dynamics in PSCs have mostly focused on the localized characterizations and analyses. Thus, it is highly desired to develop the spatially resolved techniques for understanding the in-depth loss mechanisms in PSCs. Here, we have extensively investigated the effects of dual-chloride passivation on suppressing nonradiative recombination and improving local carrier transport in PSCs. As a result, we have achieved a 25.49 cm^2 perovskite solar module with a 17.88%-certified efficiency and a record fill factor over 78%.

~1.1 V,[15–17] indicating a large V_{OC} deficit of 0.5 V for a PSC having a moderate band gap ($E_g \approx 1.6$ V), where V_{OC} deficit = $E_g/q - V_{OC}$ (q is the elementary charge). The relatively large V_{OC} deficit of PSCs is indicative of high nonradiative recombination losses. To realize efficient PSCs, high-quality perovskite films with low density of defects are required. Various methods, such as compositional engineering,[18] interfacial engineering,[19] and surface passivation,[8] have been utilized to reduce the bulk and interface defects. Thus, a wide range of additives, such as metal halide salts,[20] organic halide salts,[21] inorganic acids,[22] and nanoparticles,[23] are beneficial for assisting homogeneous nucleation or regulating crystallization kinetics.[24] Cl-contained additives have shown remarkable passivation effects,[6] including MA chloride (MACl),[25] FA chloride (FACl),[26] and cesium chloride (CsCl).[27]

However, previous studies evaluating the passivation effect and dynamics in PSCs have been mostly evidenced by comparing steady-state photoluminescence (PL) quenching or time-resolved PL (TRPL) decays,[28–31] which are the most widely utilized techniques to study the carrier lifetimes in PSCs.[32] While, these techniques only focusing on a localized position may not be considered suitable for the large-area analysis. As an alternative, luminescence imaging allows us to obtain various material and device properties in a large-scale of micrometers, such as local series resistance,[33,34] diffusion length,[35,36] and localized shunts.[37,38] Compared with the time-consuming scanning techniques, the camera-based imaging system can collect a series of luminescence images in seconds, benefiting the rapid assessment of large-scale PSCs. This fast, high-resolution, and non-destructive technique has been widely applied in silicon[33,37] and gallium arsenide (GaAs)[39] solar cells in the recent years, whereas in only a few studies on PSCs mainly focusing on the local series resistance calculation[40] and interfacial delamination identification.[41] Thus, it is highly desired to develop such advanced luminescence imaging technique to understand the in-depth optoelectronic properties of PSCs, especially those in large area.

Herein, we propose an evaluation strategy of detailing analysis on nonradiative recombination and carrier transport losses in PSCs by combining the optoelectronic reciprocity theorems with spatially resolved imaging technique. We investigate the luminescence-derived internal voltage distributions, external luminescence efficiencies, and carrier transport efficiency maps in compositionally engineered PSCs via $PbCl_2$. Upon the passivation of dual-chloride, the spatial homogeneity and film quality in a large scale are significantly enhanced. The cell shows a 1.14%external luminescence efficiency (only ~0.116 V nonradiative voltage loss) and a favorable carrier extraction property under moderate illumination level. As a result, a 17.88%-certified perovskite solar module (25.49 cm^2) with a record fill factor (FF: ~78.6%) is obtained. Our work offers a clear picture on identifying the nonradiative recombination and carrier transport losses, suggesting a feasible approach to quantitatively and spatially probe the large-area PSCs.

RESULTS AND DISCUSSION

Localized Behaviors of Perovskite Films

The control perovskite absorbers are $(CsPbI_3)_{0.05}((FAPbI_3)_{1-x}(MAPbBr_3)_x)_{0.95}$. Presence of mono-Cl in precursor benefits the passivation effects and device performance.[26,27,42] We use a 2.5% (molar ratio) $PbCl_2$ as an excess additive into MACl-incorporated precursor. The scanning electron microscope (SEM) images (Figure S1) of both control film and dual-chloride passivated film show good morphology with large grains, pinhole-free, and compact surface. The X-ray photoelectron spectroscopy (XPS) results (Figure S2) suggest no obvious increase of Cl element in the

[1]College of Materials Science and Engineering & Institute of New Energy and Low-Carbon Technology, Sichuan University, Chengdu 610065, China

[2]Institute of Fundamental and Frontier Sciences, University of Electronic Science and Technology of China, Chengdu 610054, China

[3]Chengdu R&D Center, Hanergy Thin Film Power Group Ltd., Chengdu 610200, China

[4]Research Center for Advanced Science and Technology, The University of Tokyo, Tokyo 153-8904, Japan

[5]These authors contributed equally

[6]Lead Contact

*Correspondence: hao.xia0808@scu.edu.cn (X.H.), dewei.zhao@scu.edu.cn (D.Z.)

https://doi.org/10.1016/j.joule.2020.04.013

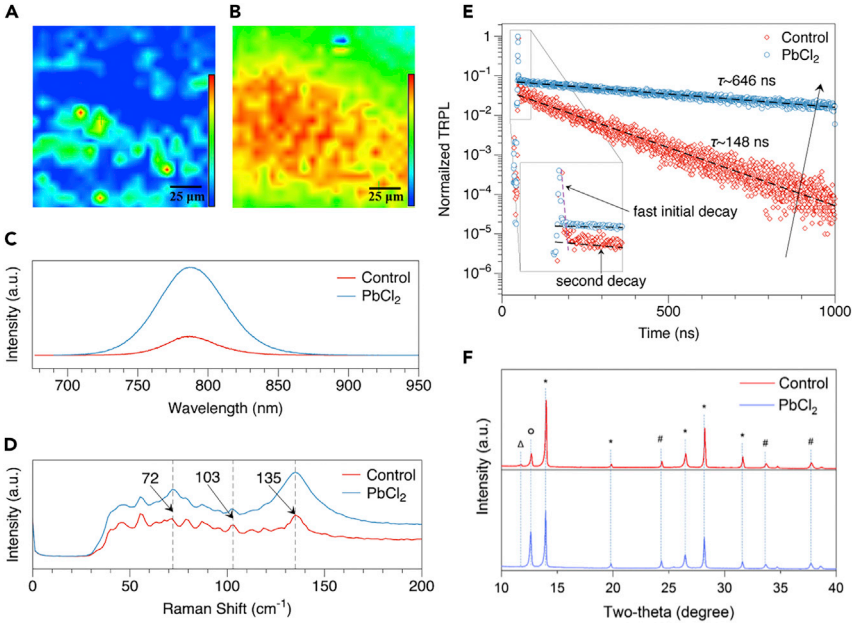

Figure 1. Localized Behaviors of Perovskite Film after Dual-Chloride Passivation

(A and B) High-resolution μ-PL imaging (200 × 200 μm^2) on (A) control and (B) $PbCl_2$-passivated perovskite films (scale bar, 25 μm).

(C and D) The (C) PL and (D) Raman spectra of both films recorded on the same localized areas in corresponding μ-PL images.

(E) The TRPL of perovskite/transport layer exhibit a bi-exponential decay, reflecting the fast charge extraction and the trap-assisted interfacial recombination. The TRPL transients demonstrate a remarkable lifetime prolongation from 148 to 646 ns after $PbCl_2$ passivation.

(F) The XRD patterns of control and $PbCl_2$-passivated perovskite films. The positions of the XRD peaks are marked with different symbols in the graphs. Note that the δ-$FAPbI_3$ yellow phase (triangle) can be only observed in the control sample, whereas the $PbCl_2$-passivated sample shows stronger PbI_2 phase (circle).

perovskite film with the incorporation of $PbCl_2$. As claimed previously, it is difficult to introduce Cl into perovskite films, since it can be easily released from the film as MACl vapor during the annealing.[43–45] In fact, Cl acts as an intermediate to control the perovskite formation processes via intramolecular exchange.[46,47]

We carried out high-resolution μ-PL imaging (200 × 200 μm^2) on two different perovskite films with the structure of fluorine-doped tin oxide (FTO)/SnO_2/perovskite. The higher PL emission behavior can be noted in μ-PL image and the extracted PL spectrum for $PbCl_2$-passivated sample (Figures 1A–1C). Moreover, both films with underneath SnO_2 exhibit the similar bi-exponential TRPL decay (Figure 1E). Specifically, the fast-initial decay (insert fitting in Figure 1E) is attributed to the rapid interface charge extraction in a few nanoseconds, and the second decay takes rather long timescales due to bulk and interface recombination. However, in this case, the fast initial decay is nondominant and can be neglected unless the transport layer completely depletes the diffusion carrier of the perovskite absorber,[32] and the carrier lifetime of the film is thereby described by the mono-exponential second decay, which indicates the ubiquity of trap-assisted recombination. As demonstrated by Tress[48] and Calado,[49] the Shockley-Read-Hall (SRH) recombination through charge trap states at bulk and interface is dominant in PSCs represented by the equation of $\frac{1}{\tau_{eff}} = \frac{1}{\tau_{rad}} + \frac{1}{\tau_{SRH}} + \cdots$, where τ_{eff} is the effective charge carrier lifetime, τ_{rad} is the radiative recombination lifetime, and τ_{SRH} is the SRH recombination lifetime. The TRPL decays demonstrate a remarkable carrier lifetime

prolongation from 148 to 646 ns, implying that the amount of nonradiative recombination loss is largely reduced upon passivation. Additionally, the Raman spectra taken on the same localized areas in μ-PL images are displayed in Figure 1D. Both perovskite films show various bands between 40 and 150 cm^{-1}, associated to the librations of hybrid organic-inorganic systems.[50,51] The ~72 cm^{-1} band is the bending and stretching mode of I–Pb–I bonds.[50,52] A weak band centered near 103 cm^{-1} can be assigned as the Raman mode of δ-$FAPbI_3$, followed by a blueshifted mode at ~135 cm^{-1} corresponding to vibrational signature of α-$FAPbI_3$ phase.[53] Note that the $PbCl_2$-passivated sample reflects an evident increase in α-phase and a slight suppression in δ-phase. Figure 1F presents X-ray diffraction (XRD) patterns of the above samples. The diffraction peak at 11.6° representing δ-$FAPbI_3$, appears in the control film and however vanishes in the film with $PbCl_2$. This result verifies that the $PbCl_2$ can effectively suppress the formation of the undesired δ-$FAPbI_3$ yellow phase that is non-photoactive. On one hand, Cl facilitates the interaction between organic cations and halide anions, resulting in lower degree of lattice distortions and shifting the density of holes and electrons away from the charge trapping states.[25,54] On the other hand, the lead-rich precursor readily forms adequate PbI_2 phase (12.6° in Figure 1F), benefiting both crystallization and morphology of the perovskite films.[55,56]

Internal Voltage Distribution and Nonradiative Recombination Losses

To further clarify the local and global influence of dual-chloride passivation on devices, we employ a direct approach to quantify the additional nonradiative recombination losses. Our PSCs have a structure of FTO/SnO_2 (25 nm)/perovskite (500 nm)/Spiro-OMeTAD (200 nm)/Au (200 nm), as shown in Figures 2A and 2B. As shown in Figure S3, the camera-based luminescence imaging systems are used to characterize the $PbCl_2$-passivated device compared with the control sample. Based on Rau's optoelectronic reciprocity relation[14] (details in the Experimental Procedures), a generalized application form to derive local internal voltage $V_i(\boldsymbol{r})$ by the original luminescence images (Figures S4 and S5) is briefly deduced in Supplemental Experimental Procedures. The derived internal voltage maps of the control and the $PbCl_2$-passivated samples exhibit large difference in distributed features and scales of the local V_i, as shown in Figures 2C and 2D. The former shows a noticeable spatial inhomogeneity in the internal voltage map and its correlated electroluminescence (EL) image (Figure S4). More specifically, a number of relatively bright and dark localized regions appear to be clustered in the internal voltage map. Similar features have also been observed in previous luminescence imaging analyses of planar PSCs.[40,57] These localized inhomogeneous regions, on the order of 10–100 micrometers, would act as potential sources of degradation within the perovskite absorber layer, hence, further deteriorate the V_{OC} and *FF* of the device.[58] In contrast, the internal voltage map of the $PbCl_2$-passivated device is almost featureless exhibiting moderate fluctuation of internal voltages, in good agreement with the results of EL images (Figure S5).

We then analyze the local value of the V_i maps, which can provide statistical verifications of the homogeneity and thus further validate the effect of $PbCl_2$ passivation. Figure 2E shows the statistical distribution of the local internal voltage of these two devices. The statistical median values of V_i for the control and $PbCl_2$-passivated devices are ~1.098 and 1.143 V, respectively. For the control sample, large fluctuations of the internal voltage values are obtained with a full width at half maximum (FWHM) of 28 mV, while the internal voltage of $PbCl_2$-passivated sample reveals an intensive distribution yielding a narrower FWHM of 8 mV. Therefore, the relatively larger average V_i and smaller FWHM of the passivated sample are strong evidences of substantially suppressed nonradiative recombination and improved homogeneity.[58] This is also consistent with the significant lifetime recovery of perovskite film

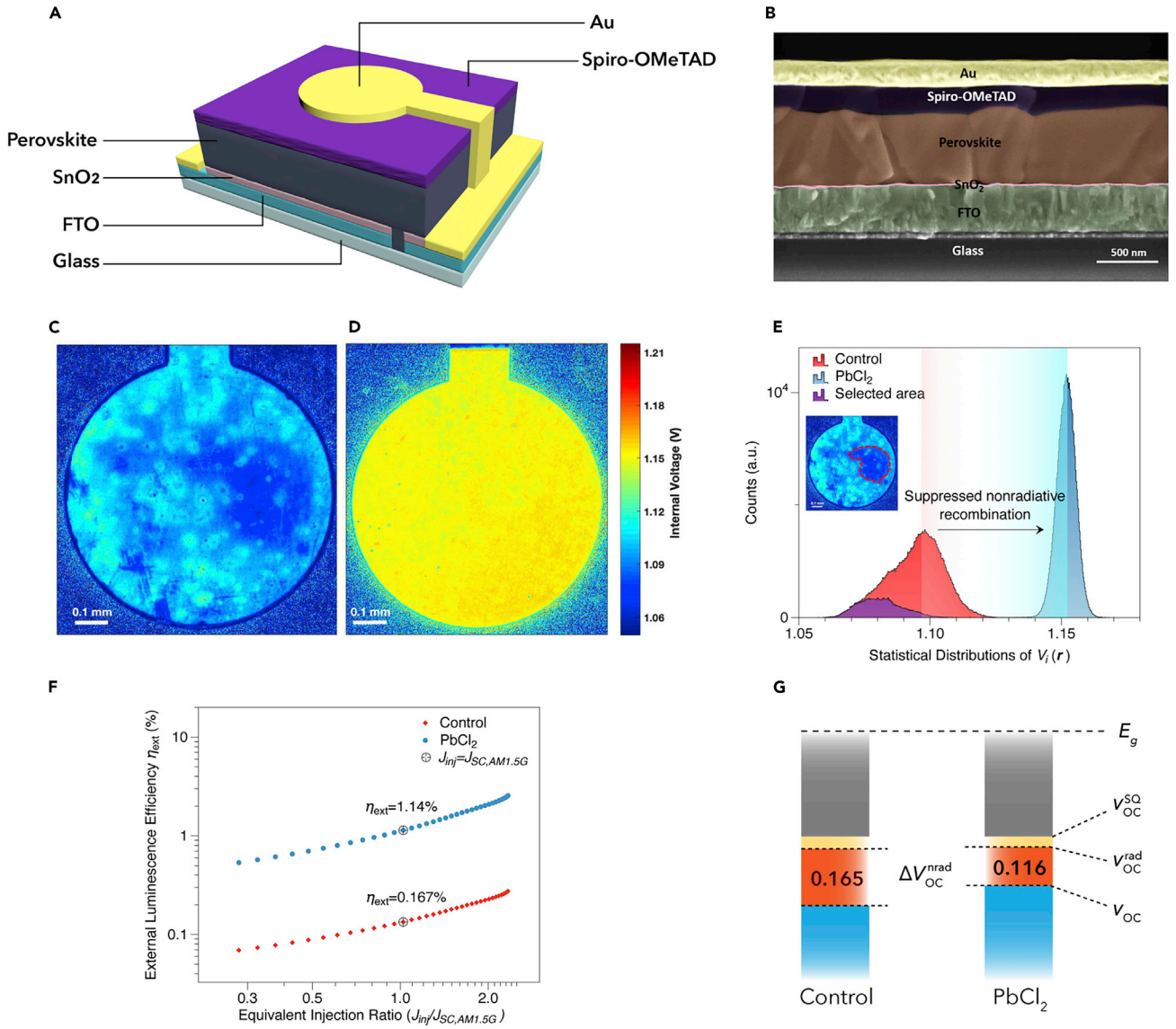

Figure 2. Derived Internal Voltage Distributions, External Luminescence Efficiencies, and Corresponding Nonradiative Recombination Losses

(A) Schematic device geometry and architecture.

(B) Cross-section SEM of a completed cell device.

(C) Internal voltage map of the control device (scale bar, 0.1 mm), which shows a noticeable spatial inhomogeneity.

(D) Internal voltage map of the $PbCl_2$-passivated devices (scale bar, 0.1 mm), which shows a moderate fluctuation and higher local internal voltage.

(E) Statistical distributions of local internal voltage counted from the V_i maps of these two devices. The statistical median values of V_i for the control and $PbCl_2$-passivated devices are ≈1.098 and 1.143 V, respectively. The insert dashed delineation denotes the selected area.

(F) The η_{ext} of control and $PbCl_2$-passivated devices as a function of the equivalent injection ratio. At 1-sun equivalent injection current density, the control and $PbCl_2$-passivated devices achieve the experimentally observed η_{ext} of 0.167% and 1.140%, respectively.

(G) The stacked bar chart of V_{OC}, V_{OC}^{rad}, V_{OC}^{SQ}, and E_g for the control and $PbCl_2$-passivated devices.

upon dual passivation. We simultaneously extract the V_i of a selected region in control sample (insert dashed delineation in Figure 3E). This defective region occupies a large fraction of floor level V_i within the sample, which tends to be forward biased by their surrounding areas and drains the current from the entire cell.

Energy losses due to the material absorbance, the non-step-function-like quantum efficiency (leading to radiative recombination below SQ gap), and nonradiative

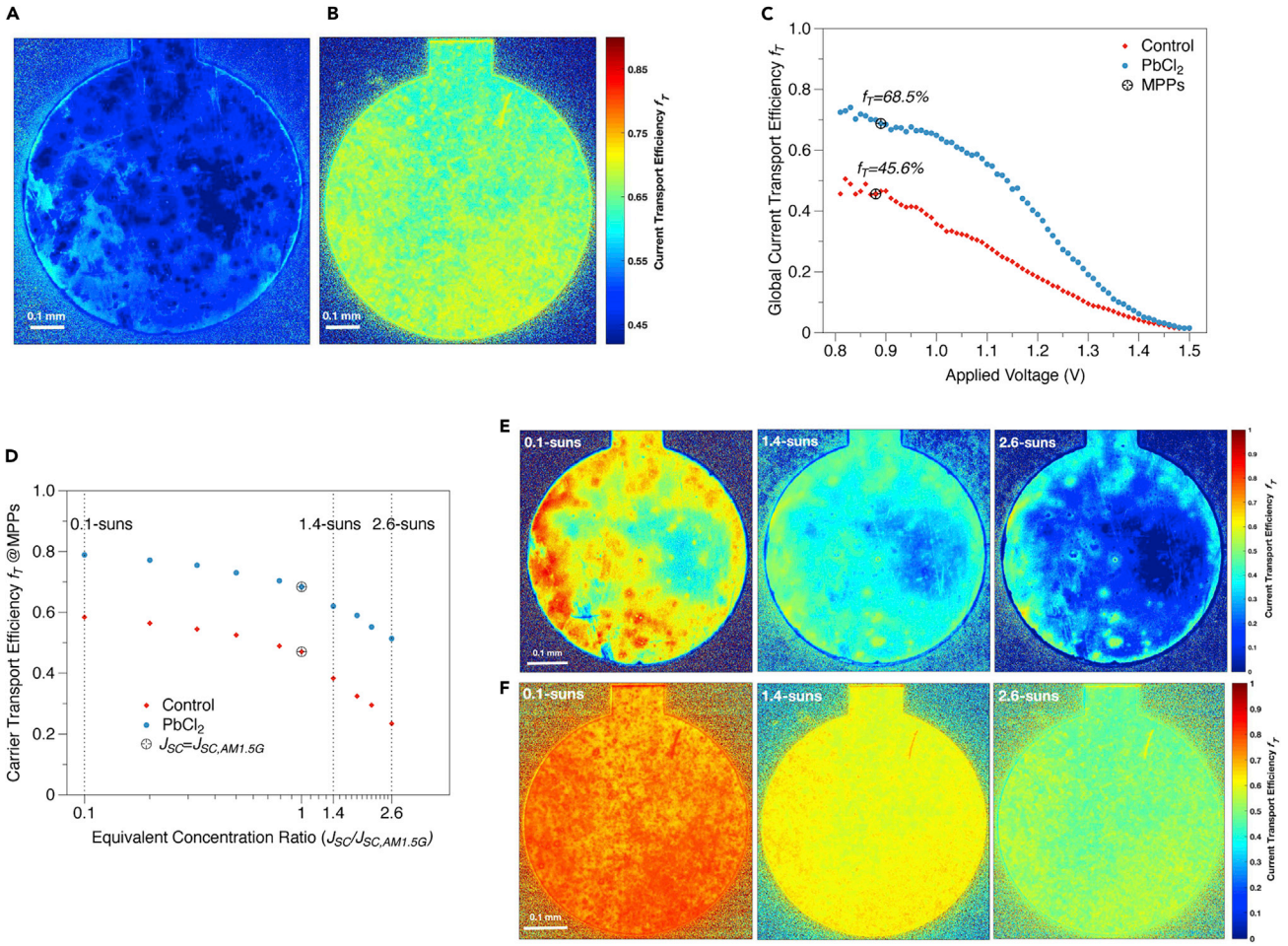

Figure 3. Local and Global Carrier Transport Performance of the Devices under Various Bias and Illumination Level

(A and B) Current transport efficiency f_T images of (A) control and (B) $PbCl_2$-passivated devices derived from the luminescence images collected at V_T = V_{MMP} with an increment of 0.01 V under 1-sun equivalent illumination (scale bar, 0.1 mm).

(C) Globally averaged f_T values of control and $PbCl_2$-passivated devices as a function of the applied voltage determined via a series of luminescence images.

(D) Global f_T values of two devices at each specific MPPs by tuning the illumination intensity from 0.1 to 2.6 suns.

(E and F) The carrier transport efficiency maps of (E) control and (F) $PbCl_2$-passivated devices under various equivalent concentration ratio. Note that the local f_T's of both devices show a downtrend as the equivalent concentration ratio raises, which is attributed to the local series resistance.

recombination, are the primary origins of the V_{OC} losses.[12] Basically, the nonradiative recombination process reduces the steady-state charge density through the recombination channel, and thus lowers the quasi-Fermi level splitting and ultimately decreases the V_{OC} of a solar cell. The quantitative relation between V_{OC} and nonradiative loss is closely connected by the external luminescence efficiency η_{ext},[59] expressed via

$$V_{OC} = V_{OC}^{rad} - \frac{kT}{q}\ln\left(\frac{1}{\eta_{ext}}\right) \qquad \text{(Equation 1)}$$

where V_{OC}^{rad} is the radiative limit to the V_{OC}. As demonstrated in our previous work,[60] we can acquire the η_{ext} as a function of the equivalent injection ratio ($J_{inj}/J_{SC,AM1.5G}$) via comparing the integrated EL spectra of samples with that of the reference cell (Figures S6–S8; Supplemental Experimental Procedures). In Figure 2F, the $PbCl_2$-passivated device achieves the η_{ext} of 1.14% at 1-sun equivalent injection current density ($J_{inj}/J_{SC,AM1.5G}$), which is about one magnitude of order higher than that of

Table 1. Summary of Key Parameters of Two Devices

Device	E_g/q (V)	V_{OC}^{rad} (V)	V_{OC} (V)	E_g/q- V_{OC} (V)	η_{ext} (Exp.)[a] (%)	$\Delta V_{OC}^{nrad,exp}$ (V)	$\Delta V_{OC}^{nrad,cal}$ (V)
Control	1.543	1.264	1.102	0.441	0.167	0.165	0.162
$PbCl_2$	1.541	1.266	1.149	0.392	1.140	0.116	0.117

[a]Note that the η_{ext} (exp.) is determined under $J_{inj} = J_{SC,1\text{-}sun}$.

the control device (0.167%). Substituting these results into Equation 1 yields the $\Delta V_{OC}^{nrad,exp}$ of 0.165 and 0.116 V for the control and $PbCl_2$- passivated devices, respectively. The increase in η_{ext}'s for both devices suggests that the nonradiative recombination rate depends less on the carrier concentration as the injection current increases. The radiative recombination, determined by the *np* product, is approximately proportional to the square of the carrier concentration in the bulk, where the excess electron concentration *n* is close to the hole concentration *p*. At a relatively higher injection level, the nonradiative recombination tends to be saturated, which leads to the increase in η_{ext}. In other words, the increase in η_{ext} with the increase in injection current indicates that the nonradiative recombination can probably occur via a limited number of recombination centers, such as trap states and dislocations.[48,61]

V_{OC}^{rad} can also be theoretically calculated by changing from a step-function like quantum efficiency (SQ case) to an experimentally measured external quantum efficiency (EQE) (radiative case)[62] (Supplemental Experimental Procedures). As shown in Table 1, the voltage losses due to the nonradiative recombination are in good agreement with those obtained from two approaches. To offer a more distinct view of V_{OC} losses in these two devices, the detailed voltage losses are summarized in a stacked bar chart (Figure 2G). The nonradiative recombination in the $PbCl_2$-passivated device is significantly suppressed without intentionally widening the band gap of absorber layer (Figure S9). As a result, we achieve a 30% reduction of nonradiative voltage losses in the passivated sample, which again corroborates the results in Figure 2E.

Bias- and Illumination-Dependent Current Transport Efficiency

Wong and Green[63] extended Donolato's reciprocity relation to a linearized equivalent theorem (details in the Experimental Procedures), where all the local current losses during the collection process within a solar cell are taken into account. This is defined as the local current transport efficiency f_T, given as follows

$$f_T(\boldsymbol{r}) = \frac{\partial I_T}{\partial I_L(\boldsymbol{r})}\Big|_{\partial V_T = 0} = \frac{\partial V_i(\boldsymbol{r})}{\partial V_T}\Big|_{\partial I_L = 0} \qquad \text{(Equation 2)}$$

where I_T is the terminal current of the cell, $I_L(\boldsymbol{r})$ is the local light-induced current, and V_T is the terminal voltage. Differentiating the logarithm of Equation 4 and substituting the result into Equation 2 yields $f_T(\boldsymbol{r}) = \partial \ln \Phi_{em}(\boldsymbol{r})/\partial(qV_T/kT)$, which implies that the spatial and quantitative f_T image can be experimentally obtained by comparing two luminescence images at incrementally different forward biases.

The f_T images of two devices (Figures 3A and 3B) are derived from the luminescence images (Figures S10 and S11) collected near each maximum power point (MPP) with an increment of 0.01 V under 1-sun equivalent illumination. A number of well-defined localized defective areas with low transport efficiencies are identified for control sample, which suggests that the generated local charge carriers are not substantially extracted to the electrodes. For the passivated sample, the recognizable spin-coating-like features are not completely eliminated in the f_T image while having

remarkable enhancement in f_T values all over the cell compared with that for the control one. The contrasting f_T behavior of two devices possibly results from a noticeable change in the contact resistance at the perovskite/SnO_2 interface. To further validate the luminescence-derived imaging results, light-beam induced current (LBIC) imaging, as an alternative spatially resolved imaging method,[57,64] is performed in these two devices (Figure S12). The measured LBIC images confirm poor local carrier extraction and transfer in the control device, especially in the central regions. In contrast, the passivated device exhibits an increase in collected local current by 65% with respect to the control one. The globally averaged f_T values of the two devices are displayed as a function of the applied voltage in Figure 3C. These values are derived by integrating the total luminescence intensity of the entire active cell area from a series of luminescence images, as reported previously.[34,39] The global f_T values of both devices drop quickly over their respective MPPs under constant illumination with increasing applied terminal voltage. The drastic decrease is attributed to the decrease in the junction resistance compared with the series resistance within the cells. It is also evident that the passivated device shows a higher global f_T (68.5%) at MPP than the control one (45.6%), indicating that the cell-level current extraction capability of the $PbCl_2$-passivated device is effectively optimized.

By tuning the illumination intensity (equivalent concentration ratio $J_{SC}/J_{SC,AM1.5G}$) from 0.1 to 2.6 suns, the global f_T values of two devices at each specific MPPs are plotted in Figure 3D. The carrier extraction efficiencies of both devices decrease dramatically for illuminations as low as 1.4 suns. In case of control device, the inhomogeneity of carrier transport is shown to be aggravated with the increase of illumination intensity (Figure 3E). Basically, the reduction of local f_T originates from the local series resistance of a solar cell.[63] These lateral inhomogeneously distributed local series resistances result from the bulk resistance of materials, sheet resistance of charge transport layer, and contact resistance between individual layers. To be specific, as the illumination intensity increases, the local current flow encounters series resistance, which enhances the junction voltage and dark current, offsetting a larger portion of the terminal current consequently. Nevertheless, introduction of the series resistance is unavoidable during the cell fabrication, even through the passivation, and the device (Figure 3F) still shows a downtrend of local f_T as the equivalent concentration ratio raises. This behavior indicates a non-negligible carrier transport loss of PSCs under high illumination levels, although the V_{OC} should continue to increase. As proven above, we note that such a method is validated at different working points (e.g., various illumination intensity and bias), thus the charge extraction capability in devices that operate closely to the actual conditions can be experimentally traced.

Photovoltaic Performance

Figure 4A shows the current density-voltage (*J-V*) curves for devices (aperture area of 0.188 cm^2) under AM1.5G 100 $mW \cdot cm^{-2}$ illumination. As expected from the mapping analysis, the $PbCl_2$-passivated device shows an enhanced PCE of 21.95% with a higher V_{OC} of 1.149 V (Table S1). For the champion device, the EQE-integrated current density over solar spectrum is 24.09 $mA \cdot cm^{-2}$, in good agreement with the short-circuit current density (J_{SC}) (24.61 $mA \cdot cm^{-2}$) from the *J-V* measurement (Figure S13). Significant improvement and reproducibility in both V_{OC} (from an average of 1.08 to 1.14 V) and efficiencies (an average value from of 20% to 22%) are achieved (Figure S14 and Table S2). Compared with the reference module (Figure S15), a 25.49 cm^2 (aperture area) perovskite module with a V_{OC} of 7.51 V, a large short-circuit current of 77.53 mA, and a high PCE of 18.73% was fabricated by dual-chloride passivation engineering, as shown in Figure 4B. Such optimized

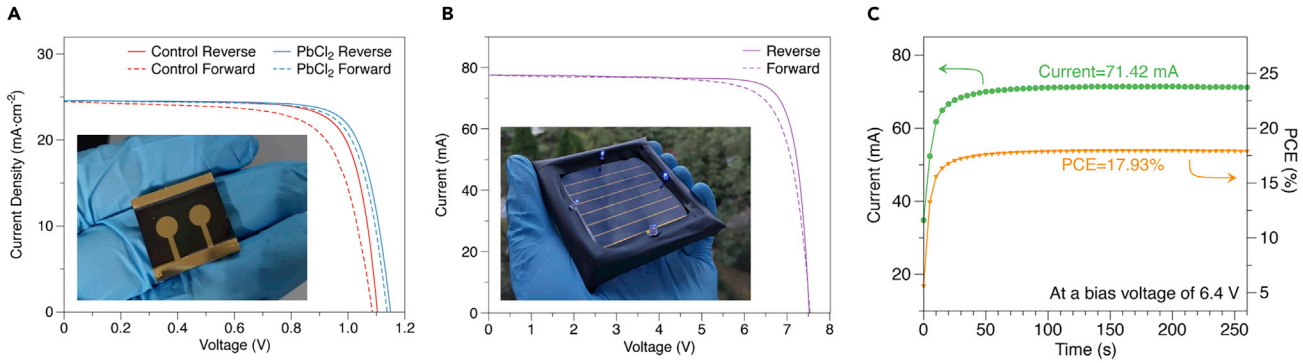

Figure 4. Device Performance of Cells and Module under Standard Conditions (AM1.5G, 100 mW·cm^{-2}, 25°C)

(A) *J-V* characteristics of the control and $PbCl_2$-passivated cells with an area of 0.188 cm^2. The insert photograph is the top view of the PSCs.

(B) *J-V* characteristics of the champion module optimized by dual-chloride passivation treatments. The insert photograph shows a 25.49 cm^2 module including 7 subcells.

(C) Module generates a stabilized PCE of 17.93%, and a current of 71.42 mA at a bias voltage of 6.4 V (near MPP).

module shows a stabilized power output efficiency with a PCE of 17.93% and a current of 71.42 mA near MPP (Figure 4C). The efficiency of our best-performing perovskite solar module was certified by an independent accredited organization (National Photovoltaic Product Quality Supervision & Inspection Center, China). The certified efficiency is 17.88% and a high FF surpasses 78% (Data S1–S3). To the best of our knowledge, this value is, thus far, the highest certified PCE and FF for ~25 cm^2 perovskite solar modules measured with an aperture area. Furthermore, we examined the long-term stability of the module under shelf storage. The V_{OC} of the optimized module showed no degradation and the PCE of the module maintained nearly ~90% of the initial value after 210 days (more than 5,000 h), exhibiting a promising shelf stability (Figure S16).

Conclusions

We have demonstrated a facile technique strategy of applying the generalized optoelectronic reciprocity relations to identify the localized and lumped origins of nonradiative recombination and carrier transport losses of PSCs through spatially resolved imaging technique. We find that nonradiative recombination in PSCs is significantly suppressed by introducing excess $PbCl_2$ additives into the MACl-incorporated precursor. Using such tunable (operating-point-dependent) method, the $PbCl_2$-passivated device shows higher efficient carrier extraction efficiency at MPP. We achieve reproducible PSCs with an average PCE close to 22% due to significant reduction in nonradiative voltage loss from 0.165 to 0.116 V. By this compositional engineering strategy, a perovskite solar module (25.49 cm^2) with a 17.88%-certified efficiency and a record FF over 78% is produced. Our work bridges the gap between the localized behavior and cell-level performance, which promises to be a powerful tool for real-time and fast assessment of PSCs in large-scale modules.

EXPERIMENTAL PROCEDURES

Resource Availability

Lead Contact

Further information and requests for resources and materials should be directed to and will be fulfilled by the Lead Contact, Dewei Zhao (dewei_zhao@hotmail.com; dewei.zhao@scu.edu.cn).

Materials Availability

This study did not generate new unique materials.

Data and Code Availability

The data presented in this work are available from the corresponding authors upon reasonable request.

Generalized Optoelectronic Reciprocity Relations

The radiative emission processes are fundamental to the operation of optoelectronic devices, especially in solar cells and light emitting diodes (LEDs). The correlation between the luminescence flux φ and quasi-Fermi level splitting $\Delta\mu$ for a photon energy E at a sample position $\boldsymbol{r}$ is described by the generalized Planck's law as follows,[65]

$$\varphi(E,\ \boldsymbol{r}) = \int_0^{\infty} \alpha(E,\ \boldsymbol{r})\varphi_{bb}(E)dE\ \exp\left(\frac{\Delta\mu}{kT}\right) \qquad \text{(Equation 3)}$$

where α is the absorptance, $\varphi_{bb}(E)$ is the black body spectrum, k is the Boltzmann constant, and T is the absolute temperature. Rau extended Equation 3 to a more practical form by giving the reciprocity relation between the luminescence emission Φ_{em} and $EQE(E,\ \boldsymbol{r})$,[14]

$$\Phi_{em}(E,\ \boldsymbol{r}) = EQE(E,\ \boldsymbol{r})\varphi_{bb}(E)\exp\left(\frac{qV_i(\boldsymbol{r})}{kT}\right) \qquad \text{(Equation 4)}$$

where kT/q is the thermal voltage. $V_i(\boldsymbol{r})$ denotes the local internal voltage of the solar cells when a terminal voltage of V_T is applied. Donolato demonstrated the relationship between the carrier collection efficiency f_c and the normalized minority carrier distribution $\delta n(\boldsymbol{r})/\delta n(j)$,[66]

$$f_c(r) = \frac{\delta n(\boldsymbol{r})}{\delta n(j)} \qquad \text{(Equation 5)}$$

where $\delta n(\boldsymbol{r})$ and $\delta n(j)$ denote the excess minority carrier density at coordinate $\boldsymbol{r}$ and the edge of space-charge region. Based on above reciprocity relations, a multiple-channel system is drawn in Figure S17, which ties together the optical input and electrical output of a solar cell/LED and vice versa. These highly symmetrical relations are vital to characterize luminescent operation of photovoltaics.

Materials

FTO glass, 7 $\Omega\ sq^{-1}$ was purchased from Nippon Sheet Glass Co., Ltd. (Japan). The tin (IV) oxide (15% in H_2O colloidal dispersion) was purchased from Alfa Aesar. Dimethylformamide (DMF, anhydrous, 99.8%), dimethyl sulfoxide (DMSO, anhydrous, >99.5%), isopropanol (anhydrous, 99.5%), chlorobenzene (anhydrous, 99.8%), acetonitrile (anhydrous, 99.8%), 4-tert-Butylpyridine (tBP, 96%), and bis(trifluoromethane)sulfonimide lithium salt (Li-TFSI, 99.95%) were purchased from Sigma Aldrich. FA iodide (FAI, anhydrous, ≥99.95%), MA bromide (MABr, anhydrous, ≥ 99.95%), MACl (anhydrous, ≥99.95%), lead (II) iodide (PbI_2, > 99.99%), cesium iodide (CsI, >99.99%), lead (II) chlorine ($PbCl_2$, >99.99%), and 2,2′,7,7′-tetrakis (N,N′-di-p-methoxyphenylamine)-9,9′-spirobifluorene (Spiro-OMeTAD, ≥99.8%) were all purchased from Xi'an Polymer Light Technology Corp., China. Au (99.999%, pellets) was purchased from Beijing Licheng Innovation Metal Materials Technology Co., Ltd., China. All the materials were used as received without post-treatment or further purification.

Device Fabrication

The pre-patterned FTO substrates (20 × 20 mm^2) were first wiped with detergent and then cleaned by sonication for 15 min in deionized water and ethanol sequentially. After drying under an N_2 stream, the substrates were cleaned by UV/ozone treatment (UVOCS Inc.) for 20 min. Then, the substrate was deposited with a

~25 nm layer of SnO_2 nanoparticle film by spin coating SnO_2 precursor (15% SnO_2 colloid diluted with deionized water) for 20 s at 4,000 rpm with a ramp rate of 2,000 rpm·s^{-1}. Then the substrate was annealed at 180°C for 20 min. The above steps were carried out in ambient air. Then the substrates were transferred into a N_2 glove box. The perovskite films were deposited by a two-step method. A stock solution of PbI_2:CsI was prepared while the $PbCl_2$ was introduced into the precursor in the form of powder. For the inorganic solution, 1.3 M of PbI_2 with 5% (molar ratio) CsI were first dissolved in mixed DMF and DMSO (volume ratio = 9:1). Then, a certain volume of the inorganic solution would be transferred into another reagent bottle and 2.5% mol of $PbCl_2$ would be added into it. The obtained solution is the PbI_2:CsI:$PbCl_2$ precursor and the remaining inorganic solution is the PbI_2:CsI precursor. For the organic precursor, 60 mg of FAI, 6 mg of MABr, and 6 mg of MACl were weighed and dissolved into 1 mL isopropanol directly. The weighing and solution preparation were done in a N_2-filled glove box. The PbI_2:CsI and PbI_2:CsI:$PbCl_2$ precursors were spin coated onto the SnO_2-coated substrates at 1,500 rpm for 30 s with a ramp rate of 1,500 rpm·s^{-1}. The resulting films were annealed at 70°C for 1 min. The organic precursor was then spin coated onto the cooled substrates at 1,700 rpm for 30 s with a ramp rate of 1,700 rpm·s^{-1}. The resulting perovskites (~500 nm) were annealed at 150°C for 15 min. 1 mL Spiro-OMeTAD solution (72.3 mg·mL^{-1} in chlorobenzene) was prepared with the addition of 18 μL Li-TFSI (520 mg·mL^{-1} in acetonitrile) and 30 μL 4-tert-butylpyridine (tBP). Spiro-OMeTAD solution was spin coated at 3,000 rpm for 30 s with a thickness of ~200 nm. The Au electrode (~200 nm) was deposited by thermal evaporation under a pressure of 4×10^{-3} Pa. The deposition rate was controlled at 0.02 nm·s^{-1} in the beginning. After 5 nm of Au layer was deposited, the deposition rate was increased to 0.15 nm·s^{-1} by increasing the evaporation power. All the fabrication processes were conducted in a N_2-filled glove box except for the deposition of Au electrode.

Module Fabrication

25.49 cm^2 perovskite solar modules with 7 subcells monolithic interconnected in series were fabricated on the FTO glass substrates with a size of 7×7 cm^2. The laser ablation process was completed by a scribing system (Wuhan Excel Science & Technology Co, Ltd., China) with a diode-pumped Q-switched frequency-doubled 532 nm Nd:YAG laser (Advanced Optowave, EST-532-1, USA). The pulse repetition frequency is 10 KHz and the pulse width is 128 ns. With laser scribing system, the series-interconnection of the module was realized by P1, P2, and P3 lines.[67] The P1 lines on FTO substrates were patterned first with an average laser power of 2.5 W. The following steps were the same as the fabrication of small-area PSCs except the volume of the precursor. The P2 lines were patterned before Au deposition with an average laser power of 0.5 W. After the thermal evaporation of Au layer, the substrates were patterned with P3 lines and the designated area of the modules were precisely defined by laser scribing with an average laser power of 0.5 W. The P1, P2, P3 scribe is 50, 150, and 150 μm, respectively. The distance between the P1-P2 scribes and the P2-P3 scribes are both controlled to be ~150 μm. The width of the interconnection area is about 0.65 mm. The width of a single subcell (including dead area) is about 7.07 mm. The geometrical FF (GFF) can be calculated as 90.8%.

Film Characterization

The film samples for the following measurements were obtained by spin coating their corresponding precursor solutions onto FTO/SnO_2. High-resolution field emission SEM images of perovskite films were taken with Hitachi S-4800. The crystal structure of perovskite films was measured using Panalytical Empyrean XRD with monochromatized Cu K_α radiation. Absorbance data of the perovskite films were

obtained by Lambda 950 UV-vis spectrophotometer (PerkinElmer Inc.). PL and TRPL measurements were performed on the perovskite films using FLS980 (Edinburgh Inc.). PL measurements were conducted using a 532-nm Xeon lamp with a monochromator while TRPL measurements were conducted using a 655-nm pico-second pulsed laser (EPL-655, 67.1 ps pulse width, 200 μm diameter). Raman spectra were obtained by using a 532 nm diode laser in continuous wave mode. An avalanche photodiode (Becker&Hickl GmbH) was used to detect the signals.

Device Characterization

The *J-V* characteristics were measured using a Keithley 2634B source meter under the illumination of a solar simulator (ABET technology) at a light intensity of 100 $mW \cdot cm^{-2}$ as checked with calibrated GaAs and silicon reference cells (NREL). The scanning rate was 100 $mV \cdot s^{-1}$, having a delay time of 100 ms and a voltage step of 10 mV. A circular aperture with a diameter of 4.9 mm (0.188 cm^2) and a rectangular aperture with a size of 49.5 × 51.5 mm^2 (25.49 cm^2) were used for measuring the cells and modules. The steady-state PCE of module was measured by setting the bias voltage to the V_{MPP} and then tracing the current density, where the V_{MPP} was set to be the same as the voltage at the MPP of the *J-V* curve.

Luminescence Imaging

The details of the luminescence imaging setups used in this paper are similar to those described in our previous publications.[34,38] The luminescence was filtered with a 670-nm long-pass filter and a 950-nm short-pass filter before the images were recorded. Then, the luminescence images were recorded by a PCO.1300 CCD camera (1,392 × 1,040 pixels) mounted on a microscope in a light-tight enclosure at room temperature (25°C). The illumination is obtained with a coherent 532-nm laser. A Keithley 2400 Sourcemeter was used as the voltage source, supplying voltage from 0.8 to 1.5 V at 0.01 V steps and 500 ms exposure time. All images were corrected for any short-circuit background noise. The schematic of the luminescence imaging setups is shown in Figure S3.

μ-PL Mapping

The μ-PL mapping measurements were carried out at room temperature with a confocal laser scanning microscope using a 635-nm diode laser (Scientex OPG-3300) for excitation. The spot size of the laser is ~2 μm. The mapping area was 200 × 200 μm^2 with a step of 8 μm in both x and y directions.

LBIC Imaging

The perovskite devices were measured using a modulated 450-nm laser (peak power = 104.6 μW), same as the one used in previous publications on characterizing moderate and wide-band-gap solar cell absorbers.[68] Here, the laser spot size is 50 μm, the switching frequency of the laser is 2,000 Hz and has a duty cycle of 50%, therefore having a pulse width of 250 μs. This laser scans the sample stage along the x axis using a Galvano scanner which was operated at a scanning frequency of 2 Hz and along the y axis by mechanical stage translation.

External Luminescence Efficiency

The EL spectra were measured by a Princeton Instruments Acton SP2300 spectrometer. The wavelengths of the Princeton spectrometer were calibrated using a supercontinuum laser. To calibrate the sensitivity of the optical system, we used an Ocean-Optics HL-3P lamp, which gives the absolute value of wavelengths (350–1,100 nm) and intensities. A CC-3 cosine adaptor slot that couples to fibers and spectrometers was used to collect signal from 180° field of view. In order to eliminate the

contribution of lower wavelengths, a 670-nm long-pass filter was used to cut needless wavelengths. The details of the experimental setups and methods can be seen in Figures S6–S8 and Supplemental Experimental Procedures.

SUPPLEMENTAL INFORMATION

Supplemental Information can be found online at https://doi.org/10.1016/j.joule.2020.04.013.

ACKNOWLEDGMENTS

The authors would like to thank Prof. Yoshitaka Okada for the LBIC measurements and Prof. Shenghao Wang for the high-resolution μ-PL imaging and Raman measurements. This work was financially supported by the Science and Technology Program of Sichuan Province (nos. 2017GZ0052, 2020YFH0079, and 2020JDJQ0030), National Energy Novel Materials Center Project (no. NENMC-I-1701), the Fundamental Research Funds for the Central Universities (nos. YJ201722 and YJ201955), and China Scholarship Council.

AUTHOR CONTRIBUTIONS

A.R., H.L., X.H., and D.Z. conceived and designed the research; A.R. performed luminescence-based imaging measurements and data analysis; H.L. carried out the device fabrication and film characterizations; X.H. and Z.T. helped to design and optimize the PSCs and modules; H.X. helped to develop and optimize the imaging measurements; B.M.F.Y.J. contributed to LBIC measurement; K.W. helped with the optical measurements; A.R. and H.L. wrote the first draft of the paper; X.H., L.W., J.Z., M.S., J.W., and D.Z. supervised the project and contributed to manuscript draft. All co-authors discussed the results and commented on the paper.

DECLARATION OF INTERESTS

The authors declare no competing interests.

Received: February 14, 2020
Revised: March 24, 2020
Accepted: April 21, 2020
Published: May 20, 2020

REFERENCES

1. National Renewable Energy Laboratory (2020). Best research-cell efficiency chart. https://www.nrel.gov/pv/cell-efficiency.html.
2. Correa-Baena, J.P., Saliba, M., Buonassisi, T., Grätzel, M., Abate, A., Tress, W., and Hagfeldt, A. (2017). Promises and challenges of perovskite solar cells. Science *358*, 739–744.
3. Chen, H., Ye, F., Tang, W., He, J., Yin, M., Wang, Y., Xie, F., Bi, E., Yang, X., Grätzel, M., and Han, L. (2017). A solvent- and vacuum-free route to large-area perovskite films for efficient solar modules. Nature *550*, 92–95.
4. Tan, H., Jain, A., Voznyy, O., Lan, X., García de Arquer, F.P.G., Fan, J.Z., Quintero-Bermudez, R., Yuan, M., Zhang, B., Zhao, Y., et al. (2017). Efficient and stable solution-processed planar perovskite solar cells via contact passivation. Science *355*, 722–726.
5. Zhao, D., Yu, Y., Wang, C., Liao, W., Shrestha, N., Grice, C.R., Cimaroli, A.J., Guan, L., Ellingson, R.J., Zhu, K., et al. (2017). Low-bandgap mixed tin-lead iodide perovskite absorbers with long carrier lifetimes for all-perovskite tandem solar cells. Nat. Energy *2*, 17018.
6. Zhao, D., Chen, C., Wang, C., Junda, M.M., Song, Z., Grice, C.R., Yu, Y., Li, C., Subedi, B., Podraza, N.J., et al. (2018). Efficient two-terminal all-perovskite tandem solar cells enabled by high-quality low-bandgap absorber layers. Nat. Energy *3*, 1093–1100.
7. Lin, R., Xiao, K., Qin, Z., Han, Q., Zhang, C., Wei, M., Saidaminov, M.I., Gao, Y., Xu, J., Xiao, M., et al. (2019). Monolithic all-perovskite tandem solar cells with 24.8% efficiency exploiting comproportionation to suppress Sn(ii) oxidation in precursor ink. Nat. Energy *4*, 864–873.
8. Jiang, Q., Zhao, Y., Zhang, X., Yang, X., Chen, Y., Chu, Z., Ye, Q., Li, X., Yin, Z., and You, J. (2019). Surface passivation of perovskite film for efficient solar cells. Nat. Photonics *13*, 460–466.
9. Anaya, M., Lozano, G., Calvo, M.E., and Míguez, H. (2017). ABX_3 perovskites for tandem solar cells. Joule *1*, 769–793.
10. Saliba, M., Matsui, T., Seo, J.Y., Domanski, K., Correa-Baena, J.P., Nazeeruddin, M.K., Zakeeruddin, S.M., Tress, W., Abate, A., Hagfeldt, A., and Grätzel, M. (2016). Cesium-containing triple cation perovskite solar cells: improved stability, reproducibility and high efficiency. Energy Environ. Sci. *9*, 1989–1997.
11. Shockley, W., and Queisser, H.J. (1961). Detailed balance limit of efficiency of p-n junction solar cells. J. Appl. Phys. *32*, 510–519.
12. Kirchartz, T., and Rau, U. (2018). What makes a good solar cell? Adv. Energy Mater. *8*, 1703385.

13. Braly, I.L., Dequilettes, D.W., Pazos-Outón, L.M., Burke, S., Ziffer, M.E., Ginger, D.S., and Hillhouse, H.W. (2018). Hybrid perovskite films approaching the radiative limit with over 90% photoluminescence quantum efficiency. Nat. Photonics *12*, 355–361.

14. Rau, U. (2007). Reciprocity relation between photovoltaic quantum efficiency and electroluminescent emission of solar cells. Phys. Rev. B *76*, 085303.

15. Singh, T., and Miyasaka, T. (2018). Stabilizing the efficiency beyond 20% with a mixed cation perovskite solar cell fabricated in ambient air under controlled humidity. Adv. Energy Mater. *8*, 1700677.

16. Wang, C., Zhang, C., Wang, S., Liu, G., Xia, H., Tong, S., He, J., Niu, D., Zhou, C., Ding, K., et al. (2018). Low-temperature processed, efficient, and highly reproducible cesium-doped triple cation perovskite planar heterojunction solar cells. Sol. RRL *2*, 1700209.

17. Thambidurai, M., Foo, S., Muhammed Salim, K.M., Harikesh, P.C., Bruno, A., Jamaludin, N.F., Lie, S., Mathews, N., and Dang, C. (2019). Improved photovoltaic performance of triple-cation mixed-halide perovskite solar cells with binary trivalent metals incorporated into the titanium dioxide electron transport layer. J. Mater. Chem. C *7*, 5028–5036.

18. Jeon, N.J., Noh, J.H., Yang, W.S., Kim, Y.C., Ryu, S., Seo, J., and Seok, S.I. (2015). Compositional engineering of perovskite materials for high-performance solar cells. Nature *517*, 476–480.

19. Zhang, J., Wang, Z., Mishra, A., Yu, M., Shasti, M., Tress, W., Kubicki, D.J., Avalos, C.E., Lu, H., Liu, Y., et al. (2020). Intermediate phase enhances inorganic perovskite and metal oxide interface for efficient photovoltaics. Joule *4*, 222–234.

20. Tang, Z., Uchida, S., Bessho, T., Kinoshita, T., Wang, H., Awai, F., Jono, R., Maitani, M.M., Nakazaki, J., Kubo, T., et al. (2018). Modulations of various alkali metal cations on organometal halide perovskites and their influence on photovoltaic performance. Nano Energy *45*, 184–192.

21. Alharbi, E.A., Dar, M.I., Arora, N., Alotaibi, M.H., Alzhrani, Y.A., Yadav, P., Tress, W., Alyamani, A., Albadri, A., Zakeeruddin, S.M., et al. (2019). Perovskite solar cells yielding reproducible photovoltage of 1.20 V. Research (Wash D C) *2019*, 8474698.

22. Heo, J.H., Song, D.H., Han, H.J., Kim, S.Y., Kim, J.H., Kim, D., Shin, H.W., Ahn, T.K., Wolf, C., Lee, T.W., and Im, S.H. (2015). Planar $CH_3NH_3PbI_3$ perovskite solar cells with constant 17.2% average power conversion efficiency irrespective of the scan rate. Adv. Mater. *27*, 3424–3430.

23. Li, S.-S., Chang, C.-H., Wang, Y.-C., Lin, C.-W., Wang, D.-Y., Lin, J.-C., Chen, C.-C., Sheu, H.-S., Chia, H.-C., Wu, W.-R., et al. (2016). Intermixing-seeded growth for high-performance planar heterojunction perovskite solar cells assisted by precursor-capped nanoparticles. Energy Environ. Sci. *9*, 1282–1289.

24. Li, T., Pan, Y., Wang, Z., Xia, Y., Chen, Y., and Huang, W. (2017). Additive engineering for highly efficient organic–inorganic halide perovskite solar cells: recent advances and perspectives. J. Mater. Chem. A *5*, 12602–12652.

25. Kim, M., Kim, G.-H., Lee, T.K., Choi, I.W., Choi, H.W., Jo, Y., Yoon, Y.J., Kim, J.W., Lee, J., Huh, D., et al. (2019). Methylammonium chloride induces intermediate phase stabilization for efficient perovskite solar cells. Joule *3*, 2179–2192.

26. Tavakoli, M.M., Yadav, P., Prochowicz, D., Sponseller, M., Osherov, A., Bulović, V., and Kong, J. (2019). Controllable perovskite crystallization via antisolvent technique using chloride additives for highly efficient planar perovskite solar cells. Adv. Energy Mater. *9*, 1803587.

27. Li, Q., Zhao, Y., Fu, R., Zhou, W., Zhao, Y., Liu, X., Yu, D., and Zhao, Q. (2018). Efficient perovskite solar cells fabricated through cscl-enhanced PbI_2 precursor via sequential deposition. Adv. Mater. *30*, e1803095.

28. Wu, Y., Yang, X., Chen, W., Yue, Y., Cai, M., Xie, F., Bi, E., Islam, A., and Han, L. (2016). Perovskite solar cells with 18.21% efficiency and area over 1 cm^2 fabricated by heterojunction engineering. Nat. Energy *1*, 16148.

29. Jiang, Q., Zhang, L., Wang, H., Yang, X., Meng, J., Liu, H., Yin, Z., Wu, J., Zhang, X., and You, J. (2017). Enhanced electron extraction using SnO_2 for high-efficiency planar-structure $HC(NH_2)_2PbI_3$-based perovskite solar cells. Nat. Energy *2*, 16177.

30. Arora, N., Dar, M.I., Hinderhofer, A., Pellet, N., Schreiber, F., Zakeeruddin, S.M., and Grätzel, M. (2017). Perovskite solar cells with CuSCN hole extraction layers yield stabilized efficiencies greater than 20%. Science *358*, 768–771.

31. Shi, J., Li, Y., Li, Y., Li, D., Luo, Y., Wu, H., and Meng, Q. (2018). From ultrafast to ultraslow: charge-carrier dynamics of perovskite solar cells. Joule *2*, 879–901.

32. Stolterfoht, M., Wolff, C.M., Márquez, J.A., Zhang, S., Hages, C.J., Rothhardt, D., Albrecht, S., Burn, P.L., Meredith, P., Unold, T., and Nehar, D. (2018). Visualization and suppression of interfacial recombination for high-efficiency large-area pin perovskite solar cells. Nat. Energy *3*, 847–854.

33. Kampwerth, H., Trupke, T., Weber, J.W., and Augarten, Y. (2008). Advanced luminescence based effective series resistance imaging of silicon solar cells. Appl. Phys. Lett. *93*, 202102.

34. Ren, A., Xu, H., Delamarre, A., Liu, C., Wu, L., Zhang, J., and Sugiyama, M. (2018). Determination of current transport efficiency map by optoelectronic reciprocity relation in CdTe solar cells. IEEE J. Photovolt. *8*, 1767–1772.

35. Würfel, P., Trupke, T., Puzzer, T., Schäffer, E., Warta, W., and Glunz, S.W. (2007). Diffusion lengths of silicon solar cells from luminescence images. J. Appl. Phys. *101*, 1650.

36. Fuyuki, T., Kondo, H., Yamazaki, T., Takahashi, Y., and Uraoka, Y. (2005). Photographic surveying of minority carrier diffusion length in polycrystalline silicon solar cells by electroluminescence. Appl. Phys. Lett. *86*, 262108.

37. Breitenstein, O., Bauer, J., Trupke, T., and Bardos, R.A. (2008). On the detection of shunts in silicon solar cells by photo- and electroluminescence imaging. Prog. Photovolt. Res. Appl. *16*, 325–330.

38. Ren, A., Xu, H., Zhang, J., Hung, H., Delamarre, A., Watanabe, K., Zhang, J., Wu, L., Liu, C., and Sugiyama, M. (2019). Spatially resolved identification of shunt defects in thin film solar cells via current transport efficiency imaging combined with 3D finite element modeling. Sol. RRL *3*, 1800342.

39. Delamarre, A., Lombez, L., Watanabe, K., Sugiyama, M., Nakano, Y., and Guillemoles, J.F. (2016). Experimental demonstration of optically determined solar cell current transport efficiency map. IEEE J. Photovolt. *6*, 528–531.

40. Walter, D., Wu, Y., Duong, T., Peng, J., Jiang, L., Fong, K.C., and Weber, K. (2018). On the use of luminescence intensity images for quantified characterization of perovskite solar cells: spatial distribution of series resistance. Adv. Energy Mater. *8*, 1701522.

41. Soufiani, A.M., Kim, J., Ho-Baillie, A., Green, M., and Hameiri, Z. (2018). Luminescence imaging characterization of perovskite solar cells: a note on the analysis and reporting the results. Adv. Energy Mater. *8*, 1702256.

42. Zhao, Y., and Zhu, K. (2014). CH_3NH_3Cl-assisted one-step solution growth of $CH_3NH_3PbI_3$: structure, charge-carrier dynamics, and photovoltaic properties of perovskite solar cells. J. Phys. Chem. C *118*, 9412–9418.

43. Chen, Q., Zhou, H., Fang, Y., Stieg, A.Z., Song, T.B., Wang, H.H., Xu, X., Liu, Y., Lu, S., You, J., et al. (2015). The optoelectronic role of chlorine in $CH_3NH_3PbI_3$(Cl)-based perovskite solar cells. Nat. Commun. *6*, 7269.

44. Mu, C., Pan, J., Feng, S., Li, Q., and Xu, D. (2017). Quantitative Doping of chlorine in formamidinium lead trihalide ($FAPbI_{3-x}Cl_x$) for planar heterojunction perovskite solar cells. Adv. Energy Mater. *7*, 1601297.

45. Unger, E.L., Bowring, A.R., Tassone, C.J., Pool, V.L., Gold-Parker, A., Cheacharoen, R., Stone, K.H., Hoke, E.T., Toney, M.F., and McGehee, M.D. (2014). Chloride in lead chloride-derived organo-metal halides for perovskite-absorber solar cells. Chem. Mater. *26*, 7158–7165.

46. Li, C., Guo, Q., Zhang, H., Bai, Y., Wang, F., Liu, L., Hayat, T., Alsaedi, A., and Tan, Z. (2017). Enhancing the crystallinity of $HC(NH_2)_2PbI_3$ film by incorporating methylammonium halide intermediate for efficient and stable perovskite solar cells. Nano Energy *40*, 248–257.

47. Yu, H., Wang, F., Xie, F., Li, W., Chen, J., and Zhao, N. (2014). The role of chlorine in the formation process of "$CH_3NH_3PbI_{3-x}Cl_x$" perovskite. Adv. Funct. Mater. *24*, 7102–7108.

48. Tress, W. (2017). Perovskite solar cells on the way to their radiative efficiency limit -insights into a success story of high open-circuit voltage and low recombination. Adv. Energy Mater. *7*, 1602358.

49. Calado, P., Burkitt, D., Yao, J., Troughton, J., Watson, T.M., Carnie, M.J., Telford, A.M., O'Regan, B.C., Nelson, J., and Barnes, P.R.F. (2019). Identifying dominant recombination

mechanisms in perovskite solar cells by measuring the transient ideality factor. Phys. Rev. Appl. *11*, 044005.

50. Quarti, C., Grancini, G., Mosconi, E., Bruno, P., Ball, J.M., Lee, M.M., Snaith, H.J., Petrozza, A., and De Angelis, F.D. (2014). The Raman spectrum of the $CH_3NH_3PbI_3$ hybrid perovskite: interplay of theory and experiment. J. Phys. Chem. Lett. *5*, 279–284.

51. Park, B.W., Jain, S.M., Zhang, X., Hagfeldt, A., Boschloo, G., and Edvinsson, T. (2015). Resonance Raman and excitation energy dependent charge transfer mechanism in halide-substituted hybrid perovskite solar cells. ACS Nano *9*, 2088–2101.

52. Gottesman, R., Gouda, L., Kalanoor, B.S., Haltzi, E., Tirosh, S., Rosh-Hodesh, E., Tischler, Y., Zaban, A., Quarti, C., Mosconi, E., and Angelis, F.D. (2015). Photoinduced reversible structural transformations in free-standing $CH_3NH_3PbI_3$ perovskite films. J. Phys. Chem. Lett. *6*, 2332–2338.

53. Steele, J.A., Yuan, H., Tan, C.Y.X., Keshavarz, M., Steuwe, C., Roeffaers, M.B.J., and Hofkens, J. (2017). Direct laser writing of δ- to α-phase transformation in formamidinium lead iodide. ACS Nano *11*, 8072–8083.

54. Nan, G., Zhang, X., Abdi-Jalebi, M., Andaji-Garmaroudi, Z., Stranks, S.D., Lu, G., and Beljonne, D. (2018). How methylammonium cations and chlorine dopants heal defects in lead iodide perovskites. Adv. Energy Mater. *8*, 1702754.

55. Kim, Y.C., Jeon, N.J., Noh, J.H., Yang, W.S., Seo, J., Yun, J.S., Ho-Baillie, A., Huang, S., Green, M.A., Seidel, J., et al. (2016). Beneficial effects of PbI_2 incorporated in organo-lead halide perovskite solar cells. Adv. Energy Mater. *6*, 1502104.

56. Liu, F., Dong, Q., Wong, M.K., Djurišić, A.B., Ng, A., Ren, Z., Shen, Q., Surya, C., Chan, W.K., Wang, J., et al. (2016). Is excess PbI_2 beneficial for perovskite solar cell performance? Adv. Energy Mater. *6*, 1502206.

57. Mastroianni, S., Heinz, F.D., Im, J.H., Veurman, W., Padilla, M., Schubert, M.C., Würfel, U., Grätzel, M., Park, N.G., and Hinsch, A. (2015). Analysing the effect of crystal size and structure in highly efficient $CH_3NH_3PbI_3$ perovskite solar cells by spatially resolved photo- and electroluminescence imaging. Nanoscale *7*, 19653–19662.

58. El-Hajje, G., Momblona, C., Gil-Escrig, L., Ávila, J., Guillemot, T., Guillemoles, J.F., Sessolo, M., Bolink, H.J., and Lombez, L. (2016). Quantification of spatial inhomogeneity in perovskite solar cells by hyperspectral luminescence imaging. Energy Environ. Sci. *9*, 2286–2294.

59. Kirchartz, T., Krückemeier, L., and Unger, E.L. (2018). Research Update: recombination and open-circuit voltage in lead-halide perovskites. APL Mater. *6*, 100702.

60. Inoue, T., Toprasertpong, K., Delamarre, A., Watanabe, K., Paire, M., Lombez, L., Guillemoles, J.-F., Sugiyama, M., and Nakano, Y. (2016). Quasi-Fermi level splitting evaluation based on electroluminescence analysis in multiple quantum-well solar cells for investigating cell performance under concentrated light. Proc. SPIE *9743*, 974316.

61. Tress, W., Marinova, N., Inganäs, O., Nazeeruddin, M.K., Zakeeruddin, S.M., and Graetzel, M. (2015). Predicting the open-circuit voltage of $CH_3NH_3PbI_3$ perovskite solar cells using electroluminescence and photovoltaic quantum efficiency spectra: the role of radiative and non-radiative recombination. Adv. Energy Mater. *5*, 1400812.

62. Qian, D., Zheng, Z., Yao, H., Tress, W., Hopper, T.R., Chen, S., Li, S., Liu, J., Chen, S., Zhang, J., et al. (2018). Design rules for minimizing voltage losses in high-efficiency organic solar cells. Nat. Mater. *17*, 703–709.

63. Wong, J., and Green, M.A. (2012). From junction to terminal: extended reciprocity relations in solar cell operation. Phys. Rev. B *85*, 235205.

64. Song, Z., Watthage, S.C., Phillips, A.B., Liyanage, G.K., Khanal, R.R., Tompkins, B.L., Ellingson, R.J., and Heben, M.J. (2015). Investigation of degradation mechanisms of perovskite-based photovoltaic devices using laser beam induced current mapping. In Proc. SPIE 9561, Thin Films for Solar and Energy Technology VII, p. 956107.

65. Würfel, P. (1982). The chemical potential of radiation. J. Phys. C: Solid State Phys. *15*, 3967–3985.

66. Donolato, C. (1985). A reciprocity theorem for charge collection. Appl. Phys. Lett. *46*, 270–272.

67. Qiu, L., Liu, Z., Ono, L.K., Jiang, Y., Son, D., Hawash, Z., He, S., and Qi, Y. (2019). Scalable fabrication of stable high efficiency perovskite solar cells and modules utilizing room temperature sputtered SnO_2 electron transport layer. Adv. Funct. Mater. *29*, 1806779.

68. Yu Jeco, B.M.F., Veinberg-Vidal, E., Vauche, L., Yoshida, K., Tamaki, R., and Ahsan, N. (2019). Luminescent coupling effect in wafer-bonded III-V on silicon multijunction solar cells. J. Photon. Energy *9*, 015504.